

BELTRAMI-NET: DOMAIN INDEPENDENT DEEP D-BAR LEARNING FOR ABSOLUTE IMAGING WITH ELECTRICAL IMPEDANCE TOMOGRAPHY (A-EIT)

S. J. HAMILTON, A. HÄNNINEN, A. HAUPTMANN, AND V. KOLEHMAINEN

ABSTRACT. *Objective:* To develop, and demonstrate the feasibility of, a novel image reconstruction method for absolute Electrical Impedance Tomography (a-EIT) that pairs deep learning techniques with real-time robust D-bar methods. *Approach:* A D-bar method is paired with a trained Convolutional Neural Network (CNN) as a post-processing step. Training data is simulated for the network using no knowledge of the boundary shape by using an associated nonphysical Beltrami equation rather than simulating the traditional current and voltage data specific to a given domain. This allows the training data to be boundary shape independent. The method is tested on experimental data from two EIT systems (ACT4 and KIT4). *Main Results:* Post processing the D-bar images with a CNN produces significant improvements in image quality measured by Structural SIMilarity indices (SSIMs) as well as relative ℓ_2 and ℓ_1 image errors. *Significance:* This work demonstrates that more general networks can be trained without being specific about boundary shape, a key challenge in EIT image reconstruction. The work is promising for future studies involving databases of anatomical atlases.

1. INTRODUCTION

Electrical Impedance Tomography (EIT) probes a body with low-amplitude electrical currents applied on surface electrodes. The surface measurements can then be used as inputs to solve a mathematical inverse problem to recover the internal electrical properties (conductivity and permittivity) of the object. As EIT is a low-cost, non-invasive imaging modality with no ionizing radiation, it has several medical and industrial applications, see [Cheney et al. (1999)] and [Mueller and Siltanen (2012)]. The image recovery task in EIT, recovering the internal conductivity from the surface electrode measurements, is a severely ill-posed nonlinear inverse problem thus requiring carefully designed reconstruction algorithms capable of handling incorrectly known boundary shape, electrode locations, and noise in the measured EIT data. The ill-posedness of the inverse problem often results in images with low spatial resolution or severe image corruption due to modeling errors in a minimization task. The D-bar method [Knudsen et al. (2009); Nachman (1996)] has been shown to be robust to modeling errors and noise [Murphy and Mueller (2009); Hamilton et al. (2018)].

By viewing these low-resolution, real-time [Dodd and Mueller (2014)], D-bar images as convolutions of the true images one can develop and train a Convolutional Neural Network (CNN) to learn the blurring inherent in the D-bar reconstruction process on data of that type. This idea was introduced in [Hamilton and Hauptmann (2018)] and tested on experimental EIT data for absolute imaging in 2D. There, the training data for the network was simulated from the forward EIT model

$$(1) \quad \begin{aligned} \nabla \cdot \sigma(z) \nabla u(z) &= 0, & z \in \Omega \subset \mathbb{R}^2 \\ \sigma \frac{\partial u}{\partial \nu} &= g, & z \in \partial\Omega \end{aligned}$$

using the electrode continuum model [Hyvönen (2009); Hauptmann (2017)] based on continuum current/voltage data computed from a known circular domain boundary. The trained network was then directly applied to D-bar reconstructions from the experimental data with no transfer training required. By contrast, here we simulate our training data from the associated, non-physical, Beltrami problem [Astala and Päiväranta (2006a,b)] and ‘Shortcut D-bar Method’ [Astala et al. (2010)] to remove any knowledge of the boundary

S. J. Hamilton is with the Department of Mathematics, Statistics, and Computer Science; Marquette University, Milwaukee, WI 53233 USA, email: sarah.hamilton@marquette.edu.

A. Hänninen is with the Department of Applied Physics; University of Eastern Finland, Kuopio, Finland, email: asko.hanninen@uef.fi.

A. Hauptmann is with the Department of Computer Science; University College London, London, United Kingdom, email: a.hauptmann@ucl.ac.uk.

V. Kohlemainen is with the Department of Applied Physics; University of Eastern Finland, Kuopio, Finland, email: ville.kolehmainen@uef.fi.

(shape and electrodes) from the training process. We test the network on EIT data from two different EIT machines (ACT4 [Liu et al. (2005)] and KIT4 [Kourunen et al. (2008)]) with different boundary shapes. In practice, a network could be constructed using a database of CT scans where all that is needed is approximate internal structure boundaries (heart, lungs, spine, etc) and reasonable conductivity value windows for each type of inclusion. The CTs could be scaled such that the maximum radial component of the thorax boundary is one. Alternatively, one could bypass any direct incorporation of organs by instead training using inclusions of ellipses, circles, etc. The patient-specific voltage and current EIT data would then be scaled to correspond to a maximum radius of 1 by scaling the associated DN (or ND) matrix by the largest radial component of the patient’s approximated boundary shape (see [Isaacson et al. (2004)]). In this study we investigate the particular question of how informative the training data needs to be in order to perform the desired image enhancement task after an initial reconstruction. That means, we consider two different scenarios in this study:

- i.) Thoracic measurements for a human patient, here a database can be built from anatomical atlases. In this setting the imaging task is highly constrained by anatomical features and hence training data can be tuned to be specific for this particular task. This constitutes a case of high *a priori* knowledge. We consider tank data with thoracic specific agar targets.
- ii.) Assessment of the most general training data without any anatomical knowledge, with which we are able to achieve sufficient reconstruction quality for a vast application area. This can be considered a task of minimizing necessary *a priori* knowledge.

The application of deep learning methods, in particular Convolutional Neural Networks (CNNs), has attracted major attention in recent years and shows great promise for improving images in tomographic reconstruction tasks. The most prominent approach is given by post-processing of an initial reconstruction based on an analytic inversion formula, such as filtered back-projection in X-ray CT [Kang et al. (2017)] and [Jin et al. (2017)]. Another promising clinical applications of this approach is dynamic cardiovascular magnetic resonance imaging [Schlemper et al. (2018); Hauptmann et al. (2018a)]. Recent studies, in addition to [Hamilton and Hauptmann (2018)], have explored the possibility of using deep learning for EIT with artificial neural networks [Martin and Choi (2017)] and variational autoencoders for lung imaging [Seo et al. (2018)]. Furthermore, several studies propose combining iterative variational techniques with deep learning to obtain superior reconstruction quality and more flexible generalization by including the forward operator in the network architectures [Adler and Öktem (2017)], [Hammernik et al. (2018)] and [Hauptmann et al. (2018b)].

Section 2 presents the methods used in this work including the proposed new algorithm and how reconstruction quality will be assessed. Results of the proposed method on experimental EIT tank data from ACT4 and KIT4 are presented in Section 3 and conclusions drawn in Section 4.

2. METHODS

Here we consider the 2D real-valued conductivity EIT problem

$$(2) \quad \nabla \cdot \sigma(z) \nabla u(z) = 0, \quad z \in \Omega \subset \mathbb{R}^2,$$

where $\sigma = \sigma(z)$ is the spatially dependent conductivity and $u = u(z)$ the electric potential. The current and voltage measurements take the form of approximate knowledge of the Neumann-to-Dirichlet (ND) map $\mathcal{R}_\sigma : \sigma \frac{\partial u}{\partial \nu} \mapsto g$ for $z \in \partial\Omega$ which maps a boundary current to the corresponding boundary voltage, and $\nu = \nu(z)$ denotes the outward unit normal vector to $\partial\Omega$. Here, for simplicity, we assume the conductivity is constant $\sigma = \sigma_0$ in a neighborhood of the boundary. If σ is not constant near $\partial\Omega$, a padding of the domain can be used as in [Nachman (1996); Siltanen and Tamminen (2016)] reducing the problem back to the case studied here.

The ND map \mathcal{R}_σ can be approximated from the measured current and voltage data with the matrix R_σ

$$(3) \quad R_\sigma(m, n) := \sum_{\ell=1}^L \frac{\phi_\ell^m v_\ell^n}{|e_\ell|}, \quad 1 \leq m, n \leq \text{num}_{LI}$$

where L denotes the number of electrodes used, num_{LI} is the number of linearly independent current patterns applied (maximum is $L - 1$), and ϕ^m , and v^n denote the normalized m -th current pattern vector and n -th

voltage vectors (see [Isaacson et al. (2004); Hamilton et al. (2018)] for scaling details). The methods described below assume the boundary conductivity $\sigma_0 = 1$ and that the domain has a maximum radial component of 1. However, if this is not the case for the measured data, the ND matrix R_σ can be scaled appropriately, as described in [Isaacson et al. (2004)], reducing the problem to the case studied here.

2.1. Intro to D-bar Methods for 2D EIT. While various D-bar based reconstruction algorithms for 2D EIT exist, they all have the same main structure:

$$[\text{CURRENT \& VOLTAGE DATA}] \xrightarrow{1} [\text{SCATTERING DATA}] \xrightarrow{2} [\text{CONDUCTIVITY}].$$

The scattering data is non-physical, and can be thought of as a nonlinear Fourier transform. The D-bar methods differ in the particular formulas used to compute the scattering data and recover the conductivity. D-bar methods come from inverse-scattering theory, an area of mathematics that brought the elegant solution to the Korteweg-de Vries (KdV) equation. D-bar methods for EIT get their name from a $\bar{\partial}$ (D-bar) equation used to recover the conductivity σ in Step 2 above.

Here we simulate our training data using using a variation of the ‘Shortcut D-bar Method’ [Astala et al. (2010)] which blends the D-bar method from the Schrödinger equation and that of the Beltrami equation. This is done to allow us to train the network using L^∞ conductivities (Beltrami method) but still reconstruct the conductivity from the scattering data using the Schrödinger $\bar{\partial}_k$ equation which [Astala et al. (2010)] suggest is more robust than Step 2 of the Beltrami method. A recent paper by Lytle et al. (2018) in fact prove that the integral equations in the Schrödinger formulation of the D-bar method hold for L^∞ conductivities which are one near $\partial\Omega$.

2.1.1. Algorithm for Simulating the Training Data. Let Ω be the unit disc. Given a set of N conductivities $\{\sigma_n\}_{n=1}^N$ in $L^\infty(\Omega)$, for each σ_n compute the associated low-pass D-bar reconstruction σ_n^{DB} as follows: 1) Generate the Beltrami scattering data $\tau(k)$ for $|k| \leq R$ for some chosen radius $R > 0$, and 2) Solve the Schrödinger $\bar{\partial}_k$ equation using the Beltrami scattering data for $|k| \leq r$ where $r \leq R$.

Step 1: Generate the Beltrami scattering data $\tau_n(k)$ for $\sigma_n(z)$ for $k \in \mathbb{C}$, $|k| \leq R$ as in [Astala et al. (2010)]

$$(4) \quad \overline{\tau_n(k)} := \frac{1}{2\pi} \int_{\mathbb{R}^2} \bar{\partial}_z [M_{+\mu_n}(z, k) - M_{-\mu_n}(z, k)] dz_1 dz_2$$

where $M_{\pm\mu_n}(z, k) = e^{-ikz} f_{\pm\mu_n}(z, k)$ are solutions to the Beltrami equation

$$(5) \quad \bar{\partial}_z f_{\pm\mu_n}(z, k) = \pm\mu_n(z) \overline{\partial_z f_{\pm\mu_n}(z, k)}$$

satisfying $M_{\pm\mu_n}(z, k) = 1 + \mathcal{O}\left(\frac{1}{|z|}\right)$ for large $|z|$ and $\mu_n(z) = \frac{1-\sigma_n(z)}{1+\sigma_n(z)}$ denotes the corresponding Beltrami coefficient.

Step 2: Relate the Beltrami and Schrödinger scattering data via $\mathbf{t}_n(k) = -4\pi i \bar{k} \tau_n(k)$, setting $\mathbf{t}_n(k) = 0$ for all $|k| > R$. Recover the low-pass D-bar reconstruction $\sigma_n^{\text{DB}} = [m_n(z, 0)]^2$ by solving the Schrödinger $\bar{\partial}_k$ equation [Knudsen et al. (2009)]

$$(6) \quad \bar{\partial}_k m_n(z, k) = \frac{1}{4\pi \bar{k}} \mathbf{t}_n(k) e(z, -k) \overline{m_n(z, k)},$$

for each $z \in [-1, 1]^2$, where $e(z, k) := \exp\{i(kz + \bar{k}\bar{z})\}$ is a unitary multiplier, using the integral form

$$(7) \quad m_n(z, \kappa) = 1 + \frac{1}{4\pi^2} \int_{\mathbb{C}} \frac{\mathbf{t}_n(k) e(z, -k)}{(\kappa - k) \bar{k}} \overline{m_n(z, k)} d\kappa_1 d\kappa_2,$$

and the computational method outlined in [Mueller et al. (2002)].

Note that no electrode or boundary information is used in the training data as $\mu_n(z) = 0$ near $\partial\Omega$. The choice of $\Omega = \mathbb{D}$ does not include boundary specific information since in the reconstruction step from experimental data, we will scale the ND map by the maximum radial component of the experimental domain Ω_{meas} , shrinking the problem to exist within our studied domain $\Omega = \mathbb{D}$. Additionally, note that the integral in (7) reduces to an integral over $|k| \leq R$ due to the compact support of $\mathbf{t}_n(k)$, and from [Nachman (1996)] $\frac{\mathbf{t}_n(k)}{k} = 0$ for $k = 0$.

2.1.2. *Recovery of Conductivity from Experimental Data.* Recover the D-bar reconstruction σ^{DB} from the measured current and voltage data via a modification to the Schrödinger \mathbf{t} ‘exp’ method as follows.

Step 1: Compute the modified Schrödinger ‘exp’ scattering data

$$\begin{aligned} \mathbf{t}^{\text{exp}}(k) &= \int_{\partial\Omega_1} e^{i\bar{k}z} (\Lambda_\sigma - \Lambda_1) e^{ikz} ds(z) \\ (8) \qquad &= \int_{\partial\Omega_1} e^{i\bar{k}z} [\Lambda_\sigma (e^{ikz}) - ik\nu e^{ikz}] ds(z), \end{aligned}$$

for $k \in \mathbb{C} \setminus 0$, $|k| \leq R_{\text{meas}}$ for some chosen radius $0 < R_{\text{meas}} \leq R$.

Step 2: Recover the D-bar conductivity reconstruction $\sigma^{\text{DB}} = (m^{\text{exp}}(z, 0))^2$ using (6) with \mathbf{t}^{exp} in place of \mathbf{t}_n , setting $\frac{\mathbf{t}^{\text{exp}}(k)}{k} = 0$ for $k = 0$.

The second line (8) comes from computing $\Lambda_1 e^{ikz} = 1 \nabla (e^{ikz}) \cdot \nu = ik\nu e^{ikz}$ which uses a continuum approximation for the DN map Λ_1 where $\nu = \nu(z)$ is the unit outward facing normal to the scaled boundary $\partial\Omega_1$ which has maximal radial component 1. The DN matrix approximation to Λ_σ is computed from $L_\sigma = (R_\sigma)^{-1}$ via (3). The DN map is also scaled by the radius of the smallest circle containing the imaged domain Ω_{meas} , and σ_0 the conductivity near the boundary $\partial\Omega_{\text{meas}}$. If σ_0 is unknown, the best constant-conductivity fit to the measured data can be used as described in [Cheney et al. (1990)]. The resulting conductivity at the end of the algorithm is then re-scaled by σ_0 . Here we compute ν numerically using a parameterization of the approximate boundary shape function (see [Hamilton et al. (2018)] for robustness studies of D-bar methods to incorrect boundary shape). Note that we only require the measured current and voltage data, approximate boundary shape of the imaged domain Ω_{meas} , and approximate locations of the electrodes for the D-bar reconstruction σ^{DB} .

2.2. Deep Learning and U-Net. In this study we follow the approach proposed in [Kang et al. (2017) and Jin et al. (2017)] for post-processing corrupted reconstructions, in our case given by the D-bar algorithm described above in Section 2.1. The methodology is motivated by the fact that the initial reconstruction is of convolutional type, such as the normal operator in CT, or in our case inversion of the truncated scattering transform. Consequently, we follow [Jin et al. (2017)] where the authors propose that a CNN can be used to remove artefacts and recover resolution loss present in the initial reconstruction. The network architectures used for this task are based on the well established U-Net [Ronneberger et al. (2015)], a multiscale autoencoder.

Let us denote the network by G_Θ , where Θ denotes the network parameters consisting of convolutional filters and biases. Then the learning task is an optimization problem to find the optimal set of parameters such that a loss function is minimized with respect to a training set. Specifically, in our case the training set is given by ground truth conductivities σ_n and D-bar reconstructions σ_n^{DB} for $n \in \mathcal{N} = \{1, \dots, N\}$, both given on the square $[-1, 1]^2$. Then the aim is to find a network that maps from D-bar reconstruction to the correct ground truth conductivity, hence we aim to find the optimal set of parameters such that

$$(9) \qquad \Theta = \arg \min_{\Theta} \sum_{n=1}^N \|G_\Theta(\sigma_n^{\text{DB}}) - \sigma_n\|_2^2.$$

The optimization is typically performed in subsets (batches) of training pairs $\{\sigma_n, \sigma_n^{\text{DB}}\}_{\mathcal{I} \subset \mathcal{N}}$, rather than the whole training set.

The chosen network architectures differ slightly depending on which task, i) or ii), of the Section 1 is considered. For scenario i.) the thoracic imaging task, we employ the same network architecture as described in [Hamilton and Hauptmann (2018)] as it has been shown to be specifically suited to reproduce structures in a known constrained environment. For task ii.) with minimal *a priori* knowledge, an assessment of network architectures was performed and we found that adding a residual connection as in [Jin et al. (2017)] increased robustness in recovering more general shapes that were not present in the training set. In both cases we kept the filter size of the convolutional kernels as 5×5 and used 4 max-pool layers, as the original U-Net architecture suggests. Networks are implemented with TensorFlow in Python.

2.3. Evaluation of the Method. To evaluate the effectiveness of our proposed Beltrami-net method we tested it on experimental data from two different EIT machines, namely, ACT4 from Rensselaer Polytechnic Institute (RPI) [Liu et al. (2005)] and KIT4 from the University of Eastern Finland (UEF) [Kourunen et al. (2008)]. We evaluate reconstruction quality using *Structural SIMilarity* Indices (SSIMs) and relative ℓ_1 and ℓ_2 image errors. The ground truth inclusion boundaries were extracted from photographs of the experiments.

As an additional comparison, we include 2D a-EIT reconstructions for the KIT4 data using a total variation (TV) regularized least squares (LS) approach. The discretized version of the problem is

$$(10) \quad \hat{\sigma} = \arg \min_{\sigma > 0} \{ \|V - U(\sigma)\|^2 + \alpha TV(\sigma) \},$$

where $\sigma \in \mathbb{R}^N$ is a piece-wise constant representation of the conductivity in a set of N pixels covering the domain Ω , $U(\sigma)$ is the finite element method (FEM) based forward solver of the complete electrode model [Somersalo et al. (1992)], α is the regularization parameter and $TV(\sigma)$ is the isotropic TV functional [Rudin et al. (1992)]

$$(11) \quad TV(\sigma) = \sum_{k=1}^N \sqrt{(\mathbf{D}_x \sigma)_i^2 + (\mathbf{D}_y \sigma)_i^2} + \beta,$$

where \mathbf{D}_x and \mathbf{D}_y are finite dimensional approximations for the partial derivatives. The minimization problem (10) is solved by using a Gauss-Newton optimization method equipped with a line search algorithm. The line search is implemented using bounded minimization such that the non-negativity $\sigma > 0$ is enforced. A detailed exposition of the method (10) can be found in [González et al. (2017)]. The regularization parameter α was tuned manually for the best visual quality of the reconstruction.

2.3.1. Experimental Data. Archival ACT4 data, taken on a circular tank of radius 15cm with 32 electrodes (width 2.5cm), was used. Agar targets with added graphite were placed in a saline bath (0.3 S/m) filled to a height of 2.25cm. Conductive and resistive targets were used to simulate the heart and aorta, as well as the lung and spine, respectively. See Figure 1 for the experimental setups. Table 1 displays the measured conductivities of the targets, using test-cells, computed via Impedimed’s SFB-7 bioimpedance meter¹. Trigonometric voltage patterns, with maximum amplitude 0.5V, were applied at a frequency of 3kHz and the resulting currents measured. For consistency with previous studies, a change of basis was performed on the measured current and voltage data to synthesize the data that would have occurred if current had been applied instead of voltage (see [Hamilton and Hauptmann (2018)]). The ND and DN matrices were then computed as described in Section 2, equation (3).

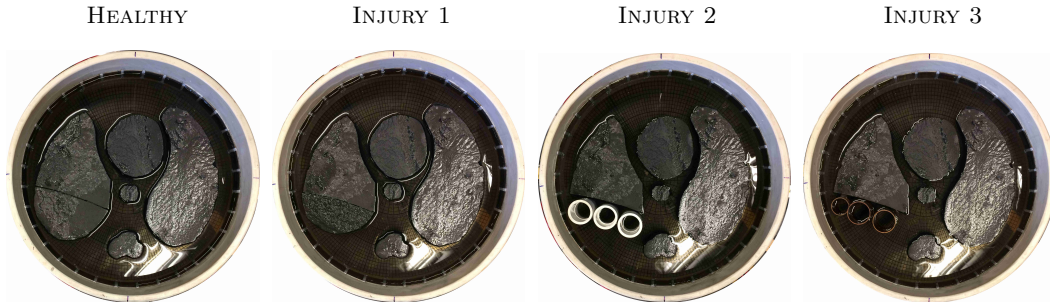


FIGURE 1. The experimental setups for the ACT4 data collection. Four scenarios were tested beginning with a ‘Healthy’ setup: conductive heart and aorta, resistive lungs and spine. In ‘Injury 1’, the bottom portion of the right (DICOM orientation) lung was removed and replaced with a conductive agar target matching the conductivity of the heart/aorta. In ‘Injury 2’, the removed portion of the right lung was replaced with three plastic pipes and for ‘Injury 3’ the removed portion is replaced with three copper pipes.

We collected KIT4 data using two different, translationally symmetric tanks to obtain data for two different boundary shapes, namely circle and chest-shaped, as shown in Figure 2. In each tank, the number

¹<https://www.impedimed.com/products/sfb7-for-body-composition/>

TABLE 1. Conductivity Values for ACT4 targets at 3.3kHz

	MEASURED VALUES (S/m)	SIMULATED VALUES Ranges (S/m)
HEART/AORTA	0.67781	[0.5, 0.8]
LUNGS/SPINE	0.056714	[0.01, 0.2]
SALINE BACKGROUND	0.3	[0.29, 0.31]
INJURY 1: AGAR/GRAPHITE	0.67781	[0.01, 1.5]
INJURY 2: PLASTIC TUBES	0	[0.01, 1.5]
INJURY 3: COPPER TUBES	infinite	[0.01, 1.5]

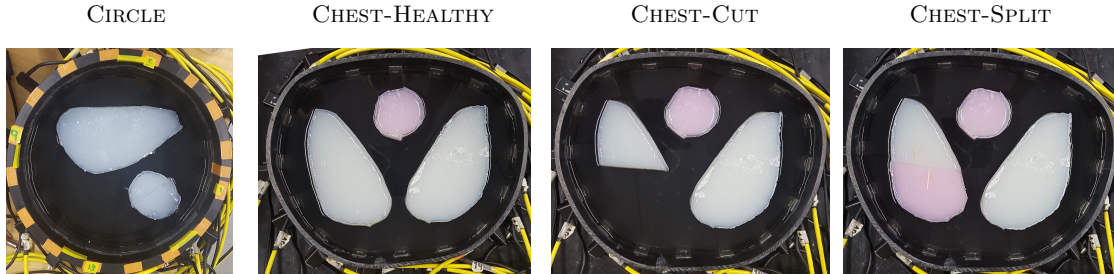


FIGURE 2. Experimental setups for the KIT4 data on three different experimental tank setups. Circle: The large object is low conductivity and small object is high conductivity. Chest: The agar targets are either high (pink) or low (white) conductivity.

of electrodes is sixteen. Adjacent (skip-0) current patterns were applied with current frequency at 10kHz and amplitude 3mA. Conductive and resistive agar targets were used across all the KIT4 experiments. The circular tank has a radius of 14cm with 16 electrodes of width 2.5cm. Agar targets of conductivity 67 mS/m (large object on the top) and 305 mS/m (smaller, nearly circular object on the bottom right) were placed in a saline bath of conductivity 135 mS/m filled to a height of 45mm. The chest shaped tank has a perimeter of 1.02m with 16 electrodes of width 2cm attached. The locations of the electrodes are not exactly equidistant from one another but can be seen from the photographs (see Figure 2). Agar targets consisting of high conductivity 323 mS/m (targets with pink ink) and low conductivity 61 mS/m (white) were placed in a saline bath (conductivity 135 mS/m, height 47mm for the *Chest-Healthy* and *Chest-Cut* targets, and 44mm for the *Chest-Split* target in Figure 2). The right (DICOM) lung was cut and two simulated injuries explored: 1) the bottom portion was removed completely (Fig. 2: *Chest-Cut*) and 2) the bottom portion was replaced with a higher conductivity piece of agar (Fig. 2: *Chest-Split*).

2.4. Training Data. Two sets of training data were used in this study, tailored to the ACT4 and KIT4 experiments. We introduce the notation $\tilde{\sigma}$ to denote a conductivity that has not yet been scaled to a boundary conductivity of 1, reserving σ solely for conductivities with a boundary value of 1.

2.4.1. ACT4 phantoms. Candidate phantoms $\tilde{\sigma}_n$ for the ACT4 training were formed by extracting the approximate boundaries of the inclusions from the ‘Healthy’ setup shown in Figure 3 (first). The approximate boundaries are shown in red * and the true boundaries are shown in black dots (Figure 3, second). Phantoms $\tilde{\sigma}_n$ were generated as follows.

- *Determine which objects are included.* Random numbers were generated from the uniform distribution on $[0, 1]$ to determine whether each inclusion (left lung: 90%, right lung: 90%, spine: 100%, heart: 95%, aorta: 95%) was included in $\tilde{\sigma}_n$.
- *Determine the conductivities of each target in $\tilde{\sigma}_n$.* The conductivities were assigned by drawing random numbers from uniform distributions using the respective conductivity windows outlined in Table 1.
- *Determine the locations of each target in $\tilde{\sigma}_n$.* The coordinates of each inclusion were created by adding noise, using the `awgn` command in MATLAB, to the ‘approximate’ coordinates (red stars) of the corresponding inclusion, see Figure 3.

As the ACT4 experiments contained ‘injuries’ to the right (DICOM) lung, simple injuries were simulated in the training data as follows. For each included lung, do the following:

- *Determine if the given lung contains an injury.* Generate a random number to determine whether or not an injury took place in the lung (50% chance).
- *If yes, divide the lung into two regions..* Create a horizontal dividing line randomly by using the max and min vertical x_2 coordinates of the lung dividing the lung into two regions.
- *Assign the injury.* Draw a random number to determine which region (top or bottom) the ‘injury’ took place (50-50 chance), and another random number drawn from the uniform distribution on the interval $[0.01, 1.5]$ to determine the conductivity of the injured region.

More complicated injuries were not considered here to allow for direct comparison to the previous study [Hamilton and Hauptmann (2018)]. Sample phantoms σ_n can be seen in Figure 3, third and fourth images.

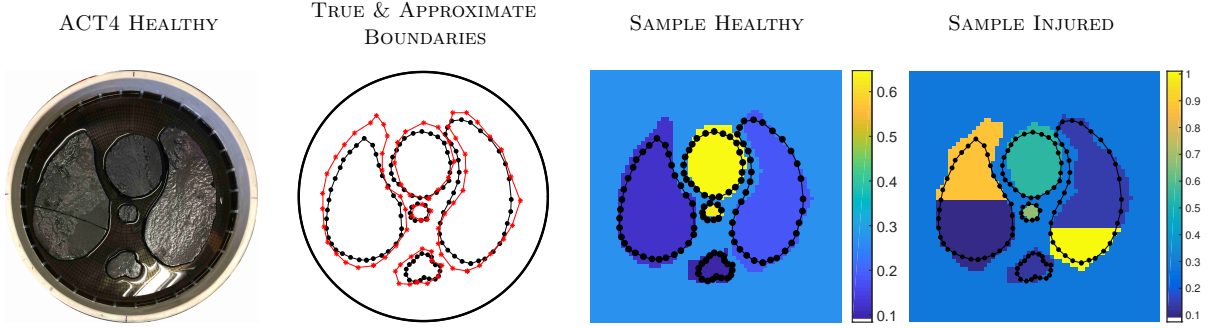


FIGURE 3. Samples of the simulated conductivities used to generate the ACT4 training data corresponding to the experiments shown in Figure 1. Starting with a healthy setup (left), the ‘true organ boundaries’ (shown in black dots) were extracted from the photograph along with an ‘approximate organ boundaries’ (red stars) which are displayed in the second image. Noise was added to these approximate boundary points to generate the organ boundaries used in the simulated conductivities. Samples of such conductivities are shown in the third and fourth images with the true organ boundaries outlined in black dots.

2.4.2. *KIT4 phantoms.* Conductivity phantoms $\tilde{\sigma}_n$ for the KIT4 training data were more general as the sizes and locations of the targets in the experiments varied greatly. Phantoms consisted of one to three ellipses of varying size (semi-major and minor axes chosen from the uniform distribution on $[0.2, 0.35]$), location $\rho e^{i\theta}$ for $\rho \in [0, 0.6]$ and $\theta \in [0, 2\pi)$, and angular orientation in $[0, 2\pi)$. The ellipses were not permitted to overlap, and were all forced to be completely contained inside a z -disc of radius 0.95. The background conductivity was chosen from the uniform distribution on the interval $[0.13, 0.145]$. For each inclusion, a random number was drawn to determine whether the inclusion was more or less conductive than the background (50-50 chance) and conductivities randomly assigned from the corresponding uniform distributions $[0.29, 0.34]$ and $[0.05, 0.075]$. The chance of a target being split into two pieces was 1 in 3. If split, no region could be smaller than 1/4 the size of the whole inclusion, and the split could be along any dividing line (horizontal, diagonal, vertical). Divided inclusions were forced to either 1) have one part match the conductivity of the background, or 2) be split into a portion that is more conductive than the background and a portion that is less conductive than the background. Sample simulated conductivities $\tilde{\sigma}_n$ are shown in Figure 6.

2.4.3. *Producing training data.* For each conductivity phantom $\tilde{\sigma}_n$, the conductivity was scaled to a boundary value of 1 via $\sigma_n = \frac{1}{\sigma_{b_n}} \tilde{\sigma}_n$ where σ_{b_n} denotes the constant conductivity near the the boundary, here the constant background value. If using a more complicated anatomical atlas, the value for σ_{b_n} would be the constant conductivity for the tissue at the patient’s boundary. Then, the conductivity is extended to $[-1, 1]^2$ by setting $\sigma_n = 1$ for $z \in [-1, 1]^2 \setminus \Omega_n$. Then, for each scaled conductivity σ_n , the Beltrami scattering data $\tau_n(k)$ (4) was computed for $|k| \leq R_{\text{ACT4}} = 5$ or $|k| \leq R_{\text{KIT4}} = 5.5$, using a $2^5 \times 2^5$ uniformly spaced k -grid on $[-5, 5]^2$ or $[-5.5, 5.5]^2$, respectively, by solving (5) with Beltrami coefficient $\mu_n(z) = \frac{1 - \sigma_n(z)}{1 + \sigma_n(z)}$ as outlined in Step 1 of Section 2.1.1. Next, the blurred D-bar reconstruction σ_n^{DB} was recovered by Step 2 of Section 2.1.1



FIGURE 4. Samples of the simulated conductivities used to generate the KIT4 training data corresponding to the experiments shown in Figure 2. One to three ellipses of varying eccentricities were randomly included with the possibility of inclusions being divided into two pieces of with no portion smaller than $1/4$ of the original inclusion.

as follows. First, the Beltrami τ_n was related to the Schrödinger \mathbf{t}_n scattering data by $\mathbf{t}_n(k) = -4\pi i \bar{k} \tau_n(k)$. Then, a random number R_n was generated for the new scattering radius cutoff from the uniform distribution on $[3.5, 5]$ for ACT4, or $[4, 5.5]$ for KIT4. Then, the computed scattering data \mathbf{t}_n was interpolated to a new $2^6 \times 2^6$ k -grid with maximum radius R_n on $[-R_n, R_n]^2$. A non-uniform cutoff threshold was enforced by setting $\mathbf{t}_n(k) = 0$ if $|\text{Re}(\mathbf{t}_n(k))|$ or $|\text{Im}(\mathbf{t}_n(k))|$ exceeded $\text{thresh} = 24$ or $|k| > R_n$. Then, the $\bar{\partial}_k$ equation was solved using the integral form (7) and the D-bar conductivity recovered as $\sigma_n^{\text{DB}}(z) = \sigma_{b_n}(m_n(z, 0))^2$, rescaling by the boundary conductivity σ_{b_n} , using a $2^6 \times 2^6$ z -grid on $[-1, 1]^2$ with gridsize $h_z \approx 0.0317$.

A total of 4,096 (ACT4) and 15,360 (KIT4) pairs $\{\tilde{\sigma}_n, \sigma_n^{\text{DB}}\}$ were created for use as training data in the U-net architectures described above in Section 2.2. Training was performed with the Adam optimizer and an initial learning rate of 10^{-4} to minimize the ℓ^2 -loss (9) with a batch size of 16 and for a total of 200,000 iterations. Training was supervised with a simulated validation set of $\sim 5\%$ of the training set size. The long training time, in terms of iterations, was mainly necessary to obtain constant areas in the inclusions as well as background. The training procedure took roughly 3 hours for each experiment on a single Nvidia Titan XP GPU.

Then, after the successful training procedure, the effectiveness was evaluated on simulated datasets σ_n^{DB} not used in the training or validation data (Section 3.1) as well as experimental reconstructions for the ACT4 and KIT4 data, applied to the respective ACT4 or KIT4 network (Section 3.2).

3. RESULTS & DISCUSSION

Here we present the results of the new Beltrami-Net method on experimental, as well as simulated, data from the ACT4 and KIT4 EIT systems.

3.1. Reconstructions from Simulated Data. We begin by visually testing the quality of the Beltrami-Net approach on simulated data. We explore test cases consistent with the training data, as well as phantoms that deviate from the procedure for creating the training set.

Figure 7 shows sample low-pass D-bar and Beltrami-Net reconstructions from simulated test data for the ACT4 scenario. As it can be seen, if the injuries are consistent with the training, at most a single horizontal dividing line in the lung as in Sims 1-2, the network can almost perfectly recover the targets. If the test data deviates from this convention, Sims 3-5, it is more difficult to recover the correct location and structure, most notably for vertical divisions. Nevertheless, for two dividing lines the network is able to locate the conductivity change correctly and establishes a sharp division in the reconstruction.

Reconstructions from simulated test data for KIT4 are shown in Figure 6. Most notably, if the inclusions are isolated and do not include a cut, the network can reconstruct these very well. We note here that the training data only included up to 3 inclusions. Nevertheless, the network seems to have no difficulties to reconstruct 4 inclusions in the image. As can be seen, the cut ellipses are more difficult to reconstruct. In most cases the network manages to include a cut in the ellipse, but in a wrong orientation. In some cases, such as simulation 5, the network is not able to distinguish between a cut and two separate inclusions.

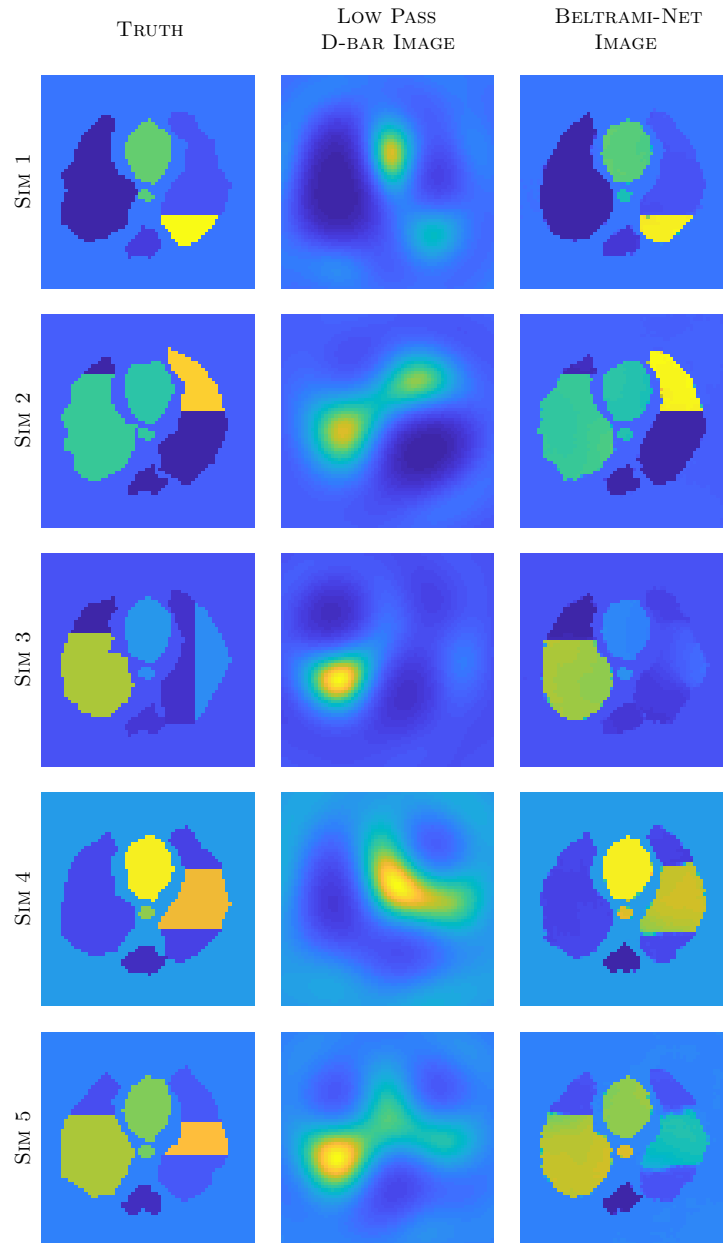


FIGURE 5. Results for simulated test data with the network trained for the ACT4 data. Note that the training data only included single horizontal divisions in the lungs. Each row is plotted on its own scale.

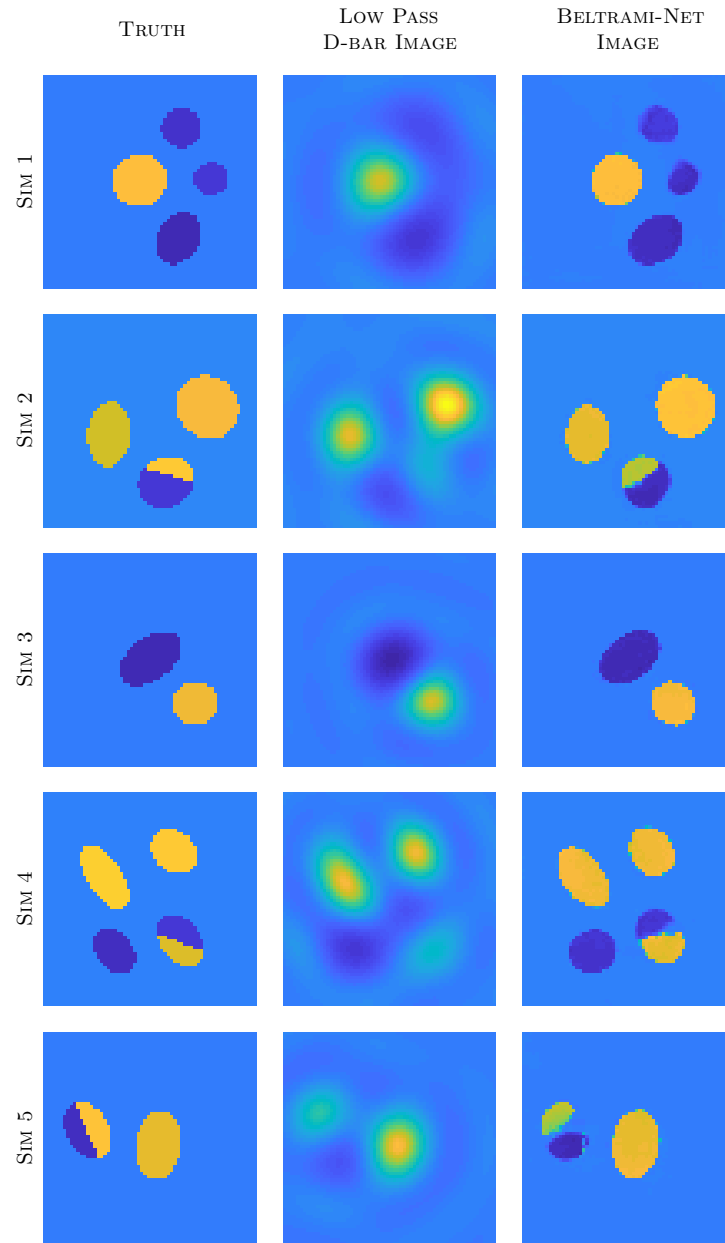


FIGURE 6. Results for simulated test data with the network trained for KIT4. Note that the training data only included up to 3 inclusions. All images are on the same scale.

3.2. Reconstructions from Experimental Data. We next present reconstructions from the ACT4 and KIT4 experimental data.

3.2.1. Experimental Reconstructions from ACT4. Figure 7 depicts the results of the *Beltrami-Net* approach on four experiments with ACT4 data: HEALTHY and INJURIES 1-3 as shown in Figure 1. The black dots represent the approximate boundaries of the ‘healthy’ organs, extracted from the photograph. SSIMs, as well as relative ℓ_1 and ℓ_2 errors, were computed for the experimental reconstructions with the exception of INJURY 3, which has infinite conductors (copper tubes). The comparisons, in Table 2, used approximate ‘truth’ images formed by assigning the measured conductivity values (Table 1) in the respective regions. Note that the coordinates for the bottom portion of the right (DICOM) lung were not specific to each injury, instead the entire region was assigned the same conductivity, even when the injury did not fill up the space as in Injury 2, plastic tubes and Injury 1 which is smaller than the original lung.

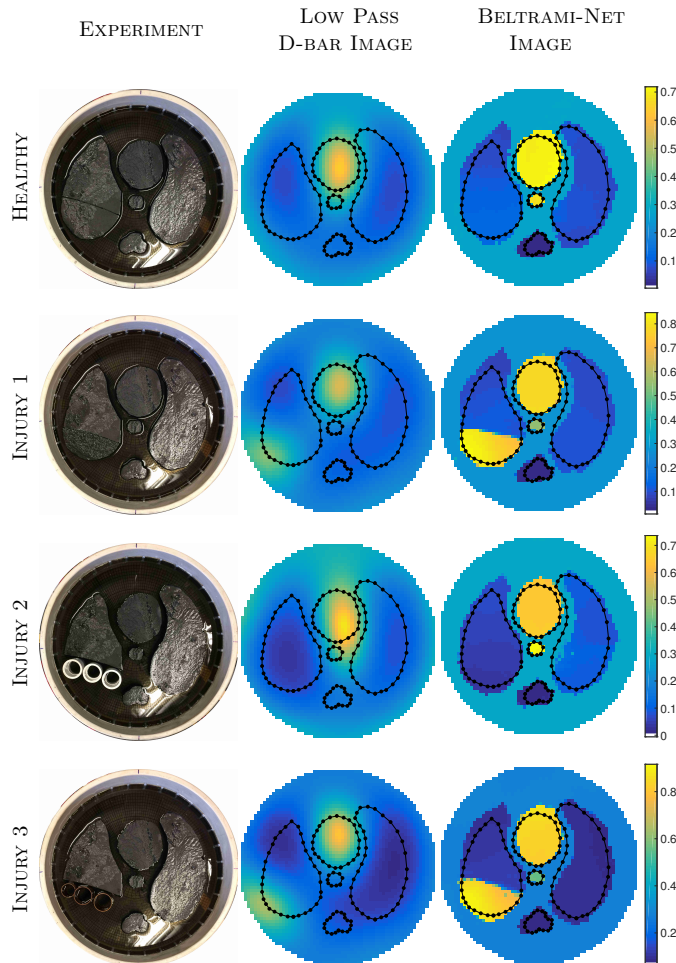


FIGURE 7. Results for the experimental ACT4 data comparing the initial low-pass D-bar images to the post-processed Deep D-bar images. Note that images are displayed here on the circular geometry of the tank, for presentation only. The D-bar images on the full square $[-1, 1]^2$ were used as inputs to the CNN to produce the Deep-Dbar images. Each row is plotted on its own scale.

The obtained reconstructions for the ACT4 scenario are overall of high quality. Visually, we can identify the injuries in the lungs clearly from the Beltrami-Net reconstructions as shown in Figure 7. Both high conductive injuries are very clearly reconstructed and are even clearly visible in the D-Bar reconstructions. The lower conductive injury is harder to identify, in the D-bar reconstruction this results in a overall lower

conductivity in the left lung. The Beltrami-Net then manages to shift the lower conductivity to bottom of the lung, but can not establish a sharp boundary. We note here, that the network was only trained on horizontal injuries, nevertheless it manages to reproduce diagonal cuts for the high conductive injuries.

Quantitatively, the Beltrami-Net reconstructions show clear improvements over the low-pass D-bar reconstructions by all metrics in Table 2. We remind here, that this is a case with strong a-priori knowledge and hence the results are expected to be of very high quality. However, unlike the previous study, [Hamilton and Hauptmann (2018)], the Beltrami-Net method did recover sharp diagonal divisions even when only training on horizontal cuts.

TABLE 2. Quantitative results for ACT4 experiments: Structural SIMilarity indices, as well as relative ℓ_1 and ℓ_2 images errors.

EXPERIMENT	LOW PASS D-BAR			BELTRAMI-NET		
	SSIM	ℓ_1 -ERROR	ℓ_2 -ERROR	SSIM	ℓ_1 -ERROR	ℓ_2 -ERROR
HEALTHY	0.5680	31.43%	22.03%	0.7296	23.75%	13.75%
AGAR	0.5176	35.87%	24.62%	0.6963	27.79%	21.01%
PLASTIC	0.5085	34.91%	24.44%	0.7053	22.26%	13.29%

3.2.2. *Experimental Reconstructions from KIT4*. We next applied the *Beltrami-Net* method to the KIT4 datasets corresponding to Figure 2 and compared to total variation regularized least squares reconstructions (TV-LS) as outlined in Section 2.3. The reconstructed images are shown in Figure 8 and quantitative measurements (SSIM and relative ℓ_1 and ℓ_2 images errors) presented in Table 3.

As one can see in Figure 8, all three methods produce images where the inclusions are clearly visible. The low-pass D-bar reconstructions are quite blurry as expected, but the post-processed images with Beltrami-Net are of very high contrast with sharp edges. In the TV-LS reconstructions, the boundary edges tend to be slightly blurred and there is a clear loss of contrast, which is a quite usual side-effect for TV regularized reconstructions. Neither of the methods is able to identify the split chest in the fourth phantom, and instead separate the lung into the two areas of opposing conductivity with saline between them. We note here that the Beltrami-Net was trained with minimal prior knowledge of only elliptic inclusions. Nevertheless, the Beltrami-Net reconstructions show shapes that differ from this simple prior. Hence we hypothesize that the network mainly learns a segmentation and correction of the existing features in the D-bar reconstructions.

The quantitative measures, SSIM, as well as relative ℓ_1 and ℓ_2 image errors, were computed for each case by comparing to approximate ‘truth’ images constructed using the measured conductivity values and photographs of the experiments, see Table 3. The quantitative improvements of Beltrami-Net are rather minor in this case. This is as expected due to low prior information. SSIM of D-Bar and Beltrami-Net are quite comparable, but generally high already. Most notably, even though the ℓ^2 -error is quite constant as well, there is a clear improvement in ℓ^1 -error, most likely due to sharper boundary edges. The TV-LS method provides comparable metrics and reconstructions, outperforming both the low-pass D-bar and Beltrami-Net methods for the SSIM of the *Chest Healthy* and *Chest Cut* phantoms, but underperforming for the *Chest Split* experiment. Most notably, the Beltrami-Net reconstruction are consistently better in ℓ^1 -error for all provided measures.

TABLE 3. Quantitative results for KIT4 experiments.

EXPERIMENT	LOW PASS D-BAR			BELTRAMI-NET			TV		
	SSIM	ℓ_1 -ERROR	ℓ_2 -ERROR	SSIM	ℓ_1 -ERROR	ℓ_2 -ERROR	SSIM	ℓ_1 -ERROR	ℓ_2 -ERROR
CIRC AGAR	0.8831	23.08%	14.39%	0.8921	19.53%	13.11%	0.8843	22.09%	16.14%
CHEST HEALTHY	0.8507	26.29%	15.73%	0.8370	21.03%	17.33%	0.8709	24.30%	17.03%
CHEST CUT	0.8684	22.56%	15.55%	0.8516	18.67%	15.26%	0.8939	20.80%	16.11%
CHEST SPLIT	0.8244	28.79%	14.76%	0.8267	21.78%	16.90%	0.7877	36.28%	36.25%

4. CONCLUSIONS

In this work we considered two conceptually different settings: i) A constrained case of thoracic imaging with the ACT4 measurements, where high a-priori knowledge is available, and ii) A very general setting with the KIT4 experiments on varying tank boundary and inclusion shapes with minimal prior knowledge in the training data. Consequently, the obtained results are slightly different in their nature. Whereas the ACT4

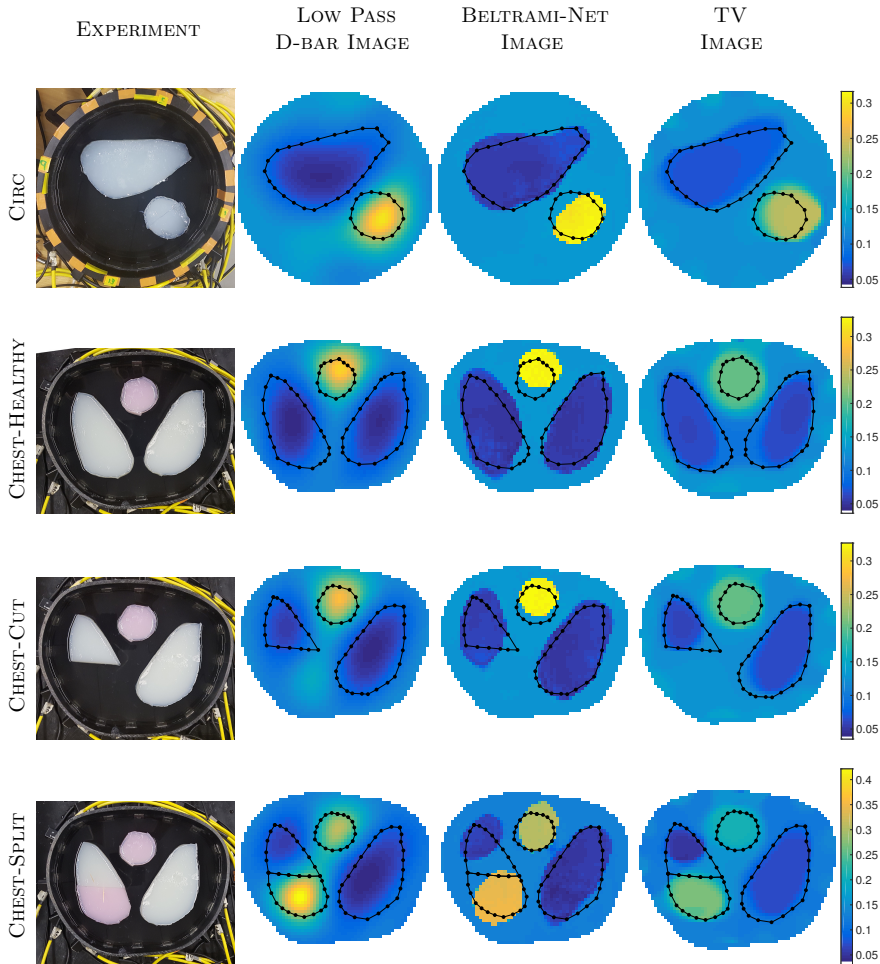


FIGURE 8. KIT4 Results for the various test scenarios. The initial D-bar image is compared to the Deep D-bar image. The D-bar images, on the full square $[-1, 1]^2$ are used as the ‘input’ images for the CNN. Images are displayed here clipped to their respective tank geometries for presentation only. Each row is plotted on its own scale.

reconstructions are of very high quality and close to the target/image prior, the KIT4 reconstructions are more general and it is harder to obtain the exact shapes of the targets. Compared to the reference method of total variation constrained least square reconstructions, the reconstruction quality of Beltrami-Net is quite similar with a slight advantage in contrast and hence ℓ^1 -error measures.

We believe that this comparison provides good insight of what is possible in EIT in combination with deep learning based post-processing, in particular for D-bar based methods. We remind here, that EIT is a highly ill-posed inverse problem and hence it is not surprising that strong prior knowledge is needed to obtain high-quality images. Thus, we believe that the presented approach will be most useful in constrained imaging settings, where boundary shapes might vary, such as thoracic imaging for the identification of lung volumes or injuries. Additionally, process monitoring and non-destructive testing, where knowledge of possible composition and defects is known, may be areas of interest for this approach.

ACKNOWLEDGEMENTS

We acknowledge the support of NVIDIA Corporation for the donation of the Titan Xp GPU used for this research. A. Hänninen and V. Kolehmainen acknowledge the Academy of Finland (Project 312343, Finnish Centre of Excellence in Inverse Modelling and Imaging) and the Jane and Aatos Erkko Foundation.

REFERENCES

- Jonas Adler and Ozan Öktem. Solving ill-posed inverse problems using iterative deep neural networks. *Inverse Problems*, 33(12):124007, 2017.
- K. Astala and L. Päivärinta. A boundary integral equation for Calderón’s inverse conductivity problem. In *Proc. 7th Internat. Conference on Harmonic Analysis, Collectanea Mathematica*, 2006a.
- K. Astala and L. Päivärinta. Calderón’s inverse conductivity problem in the plane. *Annals of Mathematics*, 163(1):265–299, 2006b. ISSN 0003-486X. doi: 10.4007/annals.2006.163.265. URL <http://dx.doi.org/10.4007/annals.2006.163.265>.
- K. Astala, J.L. Mueller, L. Päivärinta, and S. Siltanen. Numerical computation of complex geometrical optics solutions to the conductivity equation. *Applied and Computational Harmonic Analysis*, 29(1):391–403, 2010.
- M. Cheney, D. Isaacson, and E.L. Isaacson. Exact solutions to a linearized inverse boundary value problem. *Inverse Problems*, 6:923–934, 1990.
- M. Cheney, D. Isaacson, and J. C. Newell. Electrical impedance tomography. *SIAM Review*, 41(1):85–101, 1999.
- M. Dodd and J. L. Mueller. A real-time D-bar algorithm for 2-D electrical impedance tomography data. *Inverse Problems and Imaging*, 8(4):1013–1031, 2014. ISSN 1930-8337. doi: 10.3934/ipi.2014.8.1013. URL <http://aimsciences.org/journals/displayArticlesnew.jsp?paperID=10528>.
- Gerardo González, Ville Kolehmainen, and Aku Seppänen. Isotropic and anisotropic total variation regularization in electrical impedance tomography. *Computers & Mathematics with Applications*, 74(3):564 – 576, 2017. ISSN 0898-1221. doi: <https://doi.org/10.1016/j.camwa.2017.05.004>. URL <http://www.sciencedirect.com/science/article/pii/S0898122117302833>.
- S. J. Hamilton and A. Hauptmann. Deep d-bar: Real time electrical impedance tomography imaging with deep neural networks. *IEEE Transactions on Medical Imaging*, 37(10):2367–2377, 2018.
- S J Hamilton, J L Mueller, and T R Santos. Robust computation in 2d absolute eit (a-eit) using d-bar methods with the ‘exp’ approximation. *Physiological Measurement*, 39(6):064005, 2018. URL <http://stacks.iop.org/0967-3334/39/i=6/a=064005>.
- Kerstin Hammernik, Teresa Klatzer, Erich Kobler, Michael P Recht, Daniel K Sodickson, Thomas Pock, and Florian Knoll. Learning a variational network for reconstruction of accelerated mri data. *Magnetic resonance in medicine*, 79(6):3055–3071, 2018.
- A Hauptmann, S Arridge, F Lucka, V Muthurangu, and JA Steeden. Real-time cardiovascular mr with spatio-temporal artifact suppression using deep learning-proof of concept in congenital heart disease. *Magnetic resonance in medicine*, 2018a.
- Andreas Hauptmann. Approximation of full-boundary data from partial-boundary electrode measurements. *Inverse Problems*, 33(12):125017, 2017.
- Andreas Hauptmann, Felix Lucka, Marta Betcke, Nam Huynh, Jonas Adler, Ben Cox, Paul Beard, Sebastien Ourselin, and Simon Arridge. Model-based learning for accelerated, limited-view 3-d photoacoustic tomography. *IEEE transactions on medical imaging*, 37(6):1382–1393, 2018b.
- Nuutti Hyvönen. Approximating idealized boundary data of electric impedance tomography by electrode measurements. *Mathematical Models and Methods in Applied Sciences*, 19(07):1185–1202, 2009.
- D. Isaacson, J. L. Mueller, J. C. Newell, and S. Siltanen. Reconstructions of chest phantoms by the D-bar method for electrical impedance tomography. *IEEE Transactions on Medical Imaging*, 23:821–828, 2004.
- Kyong Hwan Jin, Michael T McCann, Emmanuel Froustey, and Michael Unser. Deep convolutional neural network for inverse problems in imaging. *IEEE Transactions on Image Processing*, 26(9):4509–4522, 2017.
- Eunhee Kang, Junhong Min, and Jong Chul Ye. A deep convolutional neural network using directional wavelets for low-dose x-ray ct reconstruction. *Medical physics*, 44(10), 2017.
- K. Knudsen, M. Lassas, J.L. Mueller, and S. Siltanen. Regularized D-bar method for the inverse conductivity problem. *Inverse Problems and Imaging*, 3(4):599–624, 2009.
- J Kourunen, T Savolainen, A Lehtikoinen, M Vauhkonen, and LM Heikkinen. Suitability of a pxi platform for an electrical impedance tomography system. *Measurement Science and Technology*, 20(1):015503, 2008.
- N. Liu, G.J. Saulnier, J.C. Newell, D. Isaacson, and T-J. Kao. Act4: a high-precision, multi-frequency electrical impedance tomograph. Presented at 6th Conference on Biomedical Applications of Electrical Impedance Tomography, June 2005. London, U.K.
- George Lytle, Peter Perry, and Samuli Siltanen. Nachman’s reconstruction method for the calderón problem with discontinuous conductivities. (*preprint*) *arXiv:1809.09272*, 2018.
- Sébastien Martin and Charles TM Choi. A post-processing method for three-dimensional electrical impedance tomography. *Scientific reports*, 7(1):7212, 2017.
- J.L. Mueller and S. Siltanen. *Linear and Nonlinear Inverse Problems with Practical Applications*. SIAM, 2012.
- J.L. Mueller, S. Siltanen, and D. Isaacson. A direct reconstruction algorithm for electrical impedance tomography. *IEEE Transactions on Medical Imaging*, 21(6):555–559, 2002.

- E. K. Murphy and J. L. Mueller. Effect of domain-shape modeling and measurement errors on the 2-d D-bar method for electrical impedance tomography. *IEEE Transactions on Medical Imaging*, 28(10):1576–1584, 2009.
- A. I. Nachman. Global uniqueness for a two-dimensional inverse boundary value problem. *Annals of Mathematics*, 143:71–96, 1996.
- Olaf Ronneberger, Philipp Fischer, and Thomas Brox. U-net: Convolutional networks for biomedical image segmentation. In *International Conference on Medical image computing and computer-assisted intervention*, pages 234–241. Springer, 2015.
- L.I. Rudin, S. Osher, and E. Fatemi. Nonlinear total variation based noise removal algorithms. *Physica D: Nonlinear Phenomena*, 60(1-4):259–268, 1992.
- Jo Schlemper, Jose Caballero, Joseph V Hajnal, Anthony N Price, and Daniel Rueckert. A deep cascade of convolutional neural networks for dynamic mr image reconstruction. *IEEE transactions on Medical Imaging*, 37(2):491–503, 2018.
- Jin Keun Seo, Kang Cheol Kim, Ariungerel Jargal, Kyoungun Lee, and Bastian Harrach. A learning-based method for solving ill-posed nonlinear inverse problems: a simulation study of lung eit. *arXiv preprint arXiv:1810.10112*, 2018.
- S. Siltanen and J. P. Tamminen. Reconstructing conductivities with boundary corrected d-bar method. *Journal of Inverse and Ill-posed Problems*, 22(6):847–870, 2016.
- Erkki Somersalo, Margaret Cheney, and David Isaacson. Existence and uniqueness for electrode models for electric current computed tomography. *SIAM Journal on Applied Mathematics*, 52(4):1023–1040, 1992.